Catalytic performance of MnO$_x$–NiO composite oxide in lean methane combustion at low temperature

Yagang Zhang [a,b], Zhangfeng Qin [a,*], Guofu Wang [a], Huaqing Zhu [a], Mei Dong [a], Shuna Li [a,b], Zhiwei Wu [a], Zhikai Li [a,b], Zhonghua Wu [c], Jing Zhang [c], Tiandou Hu [c], Weibin Fan [a], Jianguo Wang [a,*]

[a] State Key Laboratory of Coal Conversion, Institute of Coal Chemistry, Chinese Academy of Sciences, P.O. Box 165, Taiyuan, Shanxi 030001, PR China
[b] Graduate School of the Chinese Academy of Sciences, Beijing 100049, PR China
[c] Institute of High Energy Physics, The Chinese Academy of Sciences, Beijing 100049, PR China

ABSTRACT

A series of MnO$_x$–NiO composite oxide catalysts were prepared by co-precipitation method and used in the catalytic combustion of lean methane at low temperature. Compared with the corresponding single NiO and MnO$_x$ oxides, the MnO$_x$–NiO composite oxide with proper composition exhibits much higher catalytic performance in the lean methane oxidation. XRD and HRTEM results demonstrate that MnO$_x$–NiO is in the form of a Ni–Mn–O solid solution. XAFS and XPS results indicate that the content of manganese in MnO$_x$–NiO has a significant influence on the oxidation state of manganese and the crystal defect of nickel oxide. MnO$_x$–NiO catalyst with an atomic Mn/(Mn + Ni) ratio of 0.13 is provided with abundant highly dispersed manganese species of higher valence (Mn^{4+}) and higher coordination number as well as certain nickel vacancies, due to the strong interaction between Ni and Mn species. H$_2$-TPR and O$_2$-TPD results show that the MnO$_x$–NiO composite oxide exhibits better reducibility and oxygen mobility than NiO. All these characterizations suggest a prominent synergism between NiO and MnO$_x$ in the MnO$_x$–NiO composite oxide, which contributes to its high performance in the lean methane combustion.

© 2012 Elsevier B.V. All rights reserved.

1. Introduction

Methane is one of the most important gases that contribute towards inducing the greenhouse effect; its global warming potential is approximately 21 times higher than that of carbon dioxide [1]. Anthropogenic emissions of methane have increased markedly since pre-industrial times; most of these emissions are low concentration methane. For example, coal mining contributes 8% of anthropogenic methane emissions and 70% of these emissions come from ventilation air methane (VAM) with a concentration of 0.1–1%. It is estimated that methane emission from coal mining was over 237 MMT CO$_2$ equivalents in 2000, and increased approximately to 584 MMT CO$_2$ equivalents in 2010 [2,3]. Reducing methane emissions and producing energy from recovered methane can offer both opportunities to mitigate global climate change and to generate new sources of clean energy, which is therefore of great significance in both economic and environmental aspects.

The catalytic combustion has been considered as an effective measure to dispose lean methane for pollution abatement as well as energy utilization at low temperature [4–7]. The inert nature of methane precludes its facile oxidative destruction at low temperature. Consequently, it is crucial to design and prepare catalysts of high activity for lean methane combustion at low temperature and in recent years, a great deal of effort has been made in this respect. Among various catalyst materials used, noble metal catalysts exhibit high activity in the catalytic combustion of lean methane at low temperature [8,9]. Because of the expensiveness and rarity of noble metals, however, transition metal (Ni, Cu, Mn, Co, Fe, Cr, etc.) oxides have been considered as practical alternative materials to prepare the catalysts for the combustion of lean methane [5,10,11].

Owing to the unique redox properties, manganese oxide has exhibited excellent catalytic performance in the oxidation of CO [12], ethanol, propane [13], CH$_4$ [14], and formaldehyde oxidation [15]. The catalytic properties of manganese oxide are generally related to the variability of manganese oxidation state and the oxygen storage capacity in the crystalline lattice [13]. Moreover, the catalytic performance of manganese oxide can be enhanced significantly by adding other metal as promoter. Choudhary et al. found that the activity of Mn-doped ZrO$_2$ catalysts for methane oxidation was strongly dependent on the Mn/Zr ratio [16]. Machocki et al. reported that manganese–lanthanum oxides modified with silver showed high catalytic activity for methane oxidation; the reaction rate was a function of the surface Mn^{4+}/Mn^{3+} ratio [17]. Although

progresses have been made on the development of non-noble metal catalysts for methane combustion, their catalytic activity is in general inferior to that of noble metal catalyst at low temperature.

For the activation of reactants and proceeding of methane oxidation, a dissociative adsorption of methane and oxygen molecules is probably essential, which involves adsorption, coordination, electron transfer and dissociation processes [18]. NiO is a well-known *p*-type semiconductor with conductivity attributed to cation deficiency; the cationic vacancies induce the formation of positive holes p^+ (the main charge carriers) with Ni^{3+} or O^- ions [19]. It is then expected that the doping of NiO with manganese oxide may be beneficial to obtaining a non-noble metal catalyst of high activity for lean methane combustion.

In this work, a series of MnO_x–NiO composite oxide catalysts with various Mn/(Mn + Ni) atomic ratios were prepared by co-precipitation method and used in the catalytic combustion of lean methane at low temperature. Various characterization measures like XRD, HRTEM, XAFS, XPS, H_2-TPR and O_2-TPD were used to investigate the effect of Mn/(Mn + Ni) ratio on the interaction between nickel and manganese, the chemical state of active components, and the catalytic performance of MnO_x–NiO; moreover, on the basis of the experimental observation, the synergism between NiO and MnO_x as well as the mechanism of methane oxidation over the MnO_x–NiO composite oxide were explored.

2. Experimental

2.1. Catalyst preparation

NiO, MnO_x, and MnO_x–NiO were prepared by co-precipitation method, following the similar procedures as described elsewhere [20,21]. Briefly, a given amount of $Ni(NO_3)_2$ and $Mn(CH_3COO)_2$ were firstly dissolved in water containing 10 wt.% ethanol. The solution of $Ni(NO_3)_2$ and $Mn(CH_3COO)_2$ obtained was then hydrolyzed under stirring with aqueous Na_2CO_3 solution (2 mol/l) at 45 °C; H_2O_2 (30 wt.%) was added to oxidize Mn^{2+} to higher oxidation states. After aging and filtration, the precipitate was washed with deionized water until the pH value of filtrate reached 7.0. To drive out of water in the wet precipitate, the precipitate was then washed with a certain amount of ethanol for 3–5 times. The resulting precipitate was then dried at 110 °C for 12 h and finally calcined at 500 °C in air for 4 h. The MnO_x–NiO composite oxide catalyst prepared in this way is denoted as $MnO_x(m)$–NiO, where *m* represents the nominal atomic ratio of $n(Mn)/(n(Mn) + n(Ni))$.

2.2. Catalyst characterization

Surface area (BET) and pore diameter and volume (BJH) of the catalysts were measured by nitrogen (N_2) adsorption at −195.7 °C with a physisorption analyzer (ASAP 2000, Micromeritics Instrument Co., USA). Approximately 200 mg of the catalyst sample was used for each analysis; the samples were degassed at 200 °C and 6.7 Pa for 2 h prior to the measurement.

Elemental analysis was performed by inductively coupled plasma atomic emission spectroscopy (ICP-AES). 2 ml of concentrated nitric acid was used to dissolved 40 mg of catalyst sample, followed by adding 2 ml of 30 wt.% H_2O_2; prior to analysis, the solution was then diluted to 1000 ml with de-ionized water. By ICP-AES, the actual composition and atomic Mn/(Mn + Ni) ratio (denoted as m_{ICP}) of the $MnO_x(m)$–NiO catalysts were determined.

X-ray powder diffraction (XRD) patterns of the catalysts were collected on a powder X-ray diffractometer (Bruker AXS D8, Germany) with a monochromated Cu Kα (0.15406 nm, 40 kV, and 40 mA) radiation source. The measurements were made in the 2θ range from 5° to 85° with a scanning rate of 4°/min. The average crystallite size was estimated from the line broadening of the most intense XRD reflections by using Scherrer formula and the cell parameter of cubic NiO is obtained by the MDI Jade5 software.

High-resolution transmission electron microscopy (HRTEM) images of the catalyst were obtained on a JEM 2010 microscope operating at 200 kV and equipped with an energy-dispersive X-ray (EDX) instrument. To prepare the specimen for HRTEM, the catalyst sample was crushed to fine powder and then a holey carbon film copper grid was dipped into the crushed powder. The mean particle size is estimated from a statistic result of 100 particles randomly selected in TEM images.

Temperature programmed reduction by hydrogen (H_2-TPR) was performed in a quartz micro reactor (Tianjin-Xianquan TP-5000, China) connected with a thermal conductivity detector (TCD) and a mass spectrometer (Omni Star 200); about 50 mg of the catalyst sample (40–60 mesh) was used in each measurement. The catalyst sample was first pretreated in air (30 ml/min) at 300 °C for 1 h, followed by purging with argon (30 ml/min) at the same temperature for 1 h, and then the sample was cooled down to room temperature. After that, the flow of 10% H_2 diluted in argon (H_2–Ar mixture, 30 ml/min) was switched into the system and the sample was then heated up from room temperature to 800 °C at a ramp of 10 °C/min. The quantity of hydrogen uptake during the heating for reduction was measured by the TCD, which was calibrated by quantitative reduction of a given quantity of CuO to metallic copper.

Temperature programmed desorption of oxygen (O_2-TPD) were also performed in the quartz reactor TP-5000; 100 mg of the catalyst sample was loaded in the reactor for each measurement. The catalyst sample was first pre-treated with argon flow (30 ml/min) through heating from room temperature to 750 °C at a ramp of 10 °C/min and then oxidized with a flow of 20% O_2 in argon (O_2–Ar mixture, 30 ml/min) at 750 °C for 30 min. After that, the catalyst sample was cooled down to 50 °C in the flow of O_2–Ar mixture and then flushed with a flow of purified argon (30 ml/min) for 30 min. To perform O_2-TPD, the catalyst sample was then heated up from 50 °C to 750 °C at 10 °C/min and held at 750 °C for about 1 h; during that, the quantity of oxygen desorbed was measured by the TCD and verified by the mass spectrometry at a mass-to-charge ratio of 32.

X-ray photoelectron spectroscopy (XPS) was performed on a Quantum-2000 Scanning ESCA Microprobe electron spectrograph (Physical Electronics Company) with Al Kα radiation and a multichannel detector. Approximate 100 mg of the sample powder was compressed into a wafer for analysis. The survey spectra were measured in the binding energy (BE) range of 0–1100 eV; the detail spectra of O 1s, Mn 2p, and Ni 2p regions were measured in the ranges 520–540 eV, 630–660 eV, and 845–890 eV, respectively. The BE values were calibrated with the signal of contaminated carbon C 1s at 284.6 eV. The spectra were decomposed by using XPSPEAK software (Ver. 4.1) after applying a Shirley background subtraction and Gaussian (80%)–Lorentzian (20%) decomposition parameters. Atomic ratios were calculated from the peak areas that were calibrated by the sensitive factors provided by the equipment manufacturer.

Mn and Ni K-edge X-ray absorption spectroscopy (XAS) measurements of the catalyst samples were performed at the beam line 1W1B of Beijing Synchrotron Radiation Facility (BSRF), Institute of High Energy Physics (IHEP), Chinese Academy of Sciences (CAS). Mn and Ni K-edge XAS spectra were collected at room temperature in the transmission mode. The XAS spectra were analyzed with the program WinXAS 3.2 [22,23]. Background subtraction and normalization were performed by fitting linear polynomials to the pre-edge and the post-edge region of the absorption spectra, respectively. E_0 value was determined by the maximum in the first derivative in the edge region. The mue(0)-fit and subtraction was made by means of cubic spline fitting. Fourier transforms to *R* space

Table 1
Textural properties of $MnO_x(m)$–NiO composite oxides with different Mn contents.

m[a]	m_{ICP}[b]	Surface area (m^2/g)	Crystalline size[c] (nm)	Pore volume (cm^3/g)
0	–	25.59	40.5 (35)	0.13
0.10	0.08	78.02	22.1	0.35
0.13	0.10	112.75	17.4 (12)	0.29
0.17	0.14	55.90	29.8	0.22
0.25	0.20	46.56	30.4	0.26
1	–	49.17	85.1 (50)	0.12

[a] m is the nominal content of Mn in the composite oxide expressed as the atomic ratio of $n(Mn)/(n(Mn) + n(Ni))$.

[b] m_{ICP} is the value of the atomic ratio of $n(Mn)/(n(Mn) + n(Ni))$ determined by ICP analysis.

[c] Crystalline size is calculated from the line broadening of NiO (2 0 0) diffraction peak by the Scherrer equation from XRD patterns or estimated from the HRTEM images (digitals in brackets).

of the k^3-weighted extended X-ray absorption fine structure spectroscopy (EXAFS) data was performed for the Ni and Mn K-edge using the Gaussian window function. Pure Mn_2O_3, MnO_2, and MnO samples were used as standards to calibrate the X-ray absorption near-edge structure (XANES) of Mn species in the catalyst sample. The number of reference spectra required to reconstruct the set of XANES spectra was obtained by a principle component analysis (PCA) [23,24]. Subsequently, a linear combination fitting (LCF) procedure was applied to obtain the amounts of each reference phase from the spectra.

2.3. Catalytic reaction tests and analytic procedures

Catalytic reaction of methane combustion was carried out in a quartz tubular flow microreactor with an internal diameter of 6.0 mm at atmospheric pressure. About 200 mg of the catalyst sample (40–60 mesh) was placed at the center of the reactor using quartz glass wool as plugs and evaluated in the fresh state without any pretreatment. The feed stream consisted of 1.0 vol.% CH_4, 19 vol.% O_2, and balanced argon; and the weight hourly space velocity (WHSV) of the feed stream was 32 000 ml g^{-1} h^{-1}. After the reacting stream entered the reactor at room temperature, a light-off test (temperature-programmed reaction) was conducted at a heating rate of 2 °C/min until CH_4 was completely converted into CO_2 and H_2O, to evaluate the catalyst activity for methane combustion. In the light-off profiles, the temperatures corresponding to methane conversions of 10%, 50%, and 90% are designated as T_{10}, T_{50}, and T_{90}, respectively.

CH_4 and CO_2 in the effluent gas were periodically analyzed online with a gas chromatograph (Shimadzu GC-2010) equipped with a column packed with carbon molecular sieve, a post-column methanator that converted CO_2 into CH_4, and a flame ionization detector (FID).

3. Results and discussion

3.1. Catalyst characterization

3.1.1. Textural properties, XRD and HRTEM results

Specific surface area, particle size and pore volume of the $MnO_x(m)$–NiO catalysts with different m values (i.e. the atomic ratio of $n(Mn)/(n(Mn) + n(Ni))$, representing the content of Mn in the composite oxide), estimated from physical sorption of nitrogen and XRD measurement, are listed in Table 1. The $MnO_x(m)$–NiO composite oxide exhibits higher surface area and smaller particle size than the single pure oxides of MnO_x and NiO. Especially, when the value of m is 0.13, $MnO_x(0.13)$–NiO shows the largest surface area and the smallest particle size, implying that the addition of appropriate amount of manganese is of benefit to inhibiting
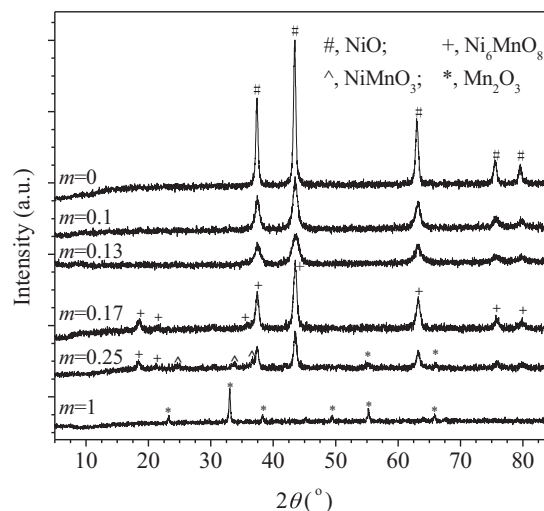

Fig. 1. XRD patterns of $MnO_x(m)$–NiO composite oxides with different Mn contents ($m = n(Mn)/(n(Mn) + n(Ni))$).

NiO crystallite from growing up during preparation. Similar phenomenon has also been observed for Mn–Co [10] and Mn–Ce catalysts [25].

XRD patterns of the $MnO_x(m)$–NiO catalysts are shown in Fig. 1. For the single pure oxide of MnO_x, intensive and sharp diffraction peaks at 2θ of 23.3°, 33.0°, 38.3°, 49.5°, 55.2° and 65.9° observed here can be primarily attributed to α-Mn_2O_3 (JCPDS 65-7467). α-Mn_2O_3 is generally considered as a mixture of crystalline Mn_2O_3 (bixbyite) and MnO_2; the former that involves Mn^{3+} ion is the dominant component, while the later that involves Mn^{4+} ion is much less [26]. For the single pure oxide of NiO, the diffraction peaks at 2θ of 37.4°, 43.4°, 63.0°, 75.6° and 79.5° are ascribed to the cube spinel structure of NiO (JCPDS 75-0197).

After the doping of manganese species into NiO, the diffraction peaks for NiO are broadened and their intensity is also largely decreased, indicating that NiO oxide doped with manganese has a much smaller crystal size than pure NiO, which is consistent with the results of nitrogen sorption (Table 1). Besides, smaller crystallites may also mean the presence of more crystal defects which are catalytic active for certain reactions.

As shown in Fig. 1, only crystalline NiO phase is detected by XRD in the $MnO_x(m)$–NiO composite oxide with low manganese content (when the value of m, i.e. the atomic ratio of Mn/(Mn + Ni) does not exceed 0.13). With further increase of the manganese content, new manganese species are emerged in $MnO_x(m)$–NiO. When m is 0.17, a new phase attributed to Ni_6MnO_8 composite oxide with the diffraction peaks at 2θ of 18.5°, 21.2°, 37.5°, 43.5°, 63.2°, 75.8°, and 80.0° (JCPDS 83-1186) is observed. Mn^{4+} that can supply oxygen vacancies is involved in Ni_6MnO_8 [27], which may contribute to the activity of manganese-containing catalysts for methane oxidation [17]. When the value of m reaches 0.25, the $MnO_x(0.25)$–NiO composite oxide shows similar diffraction peaks corresponding to Ni_6MnO_8; besides that, trace amounts of $NiMnO_3$ (JCPDS 75-2089) and Mn_2O_3 crystalline are also observed. There is little large crystalline species of Mn_2O_3 in the $MnO_x(m)$–NiO composite oxide as detected by XRD, even though the value of m reaches 0.25. These suggest that with the addition of manganese, a Mn–Ni–O solid solution is formed. Because the radius of Mn^{3+} (0.066 nm) and Mn^{4+} (0.056 nm) are smaller than that of Ni^{2+} (0.069 nm), the solid solution may be obtained through the insertion of a portion of Mn^{3+} and Mn^{4+} ions into the lattice of NiO. Moreover, the very weak diffraction peaks attributed to Mn_2O_3 in $MnO_x(m)$–NiO strongly suggests that Mn_2O_3 is amorphous or highly dispersed into the lattice of NiO. Fig. 1 also suggests that excessive doping of MnO_x
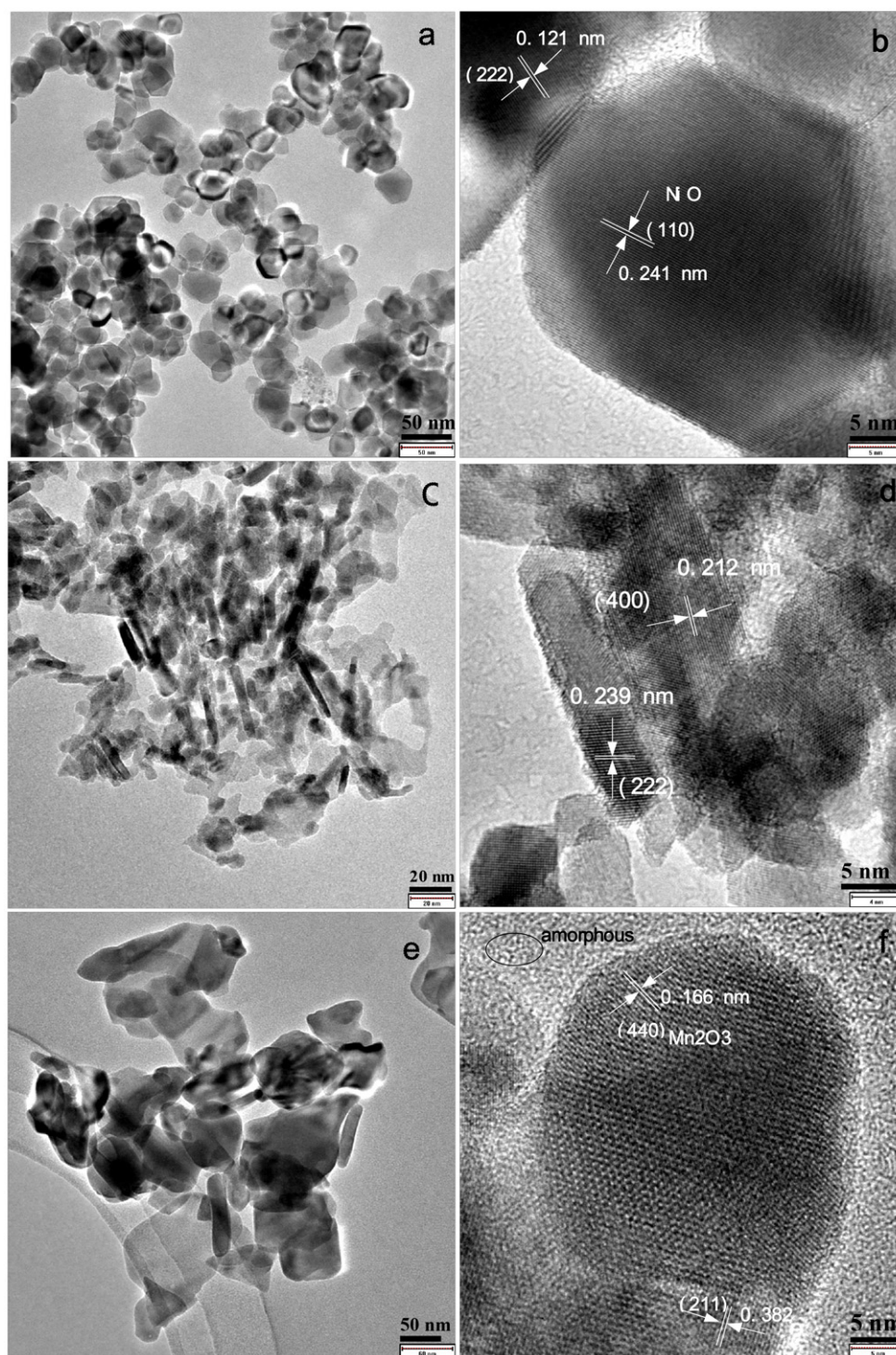
Fig. 2. TEM and HRTEM images of $MnO_x(m)$–NiO composite oxides with different Mn contents: (a) and (b), $m = 0$; (c) and (d), $m = 0.13$; (e) and (f), $m = 1$.

into NiO ($m > 0.17$) may lead to the formation of Mn_2O_3 crystallite, which is not favorable for the formation of solid solution; over-doped Mn species cannot be incorporated into the lattice of NiO and may congregate as Mn_2O_3 phase on the nickel oxide surface.

Since the diffraction peaks of Ni_6MnO_8 are partially overlapped with those of NiO, it is some difficult to distinguish between Ni_6MnO_8 and NiO phases in $MnO_x(m)$–NiO by XRD. Hence HRTEM is further used to observe the structure and composition of $MnO_x(m)$–NiO (Fig. 2). As shown in Fig. 2(a), pure NiO ($m = 0$) is composed of polyhedra with irregular shapes; the mean particle

size is about 40 nm, as calculated from the XRD data by Scherrer's equation. The magnified HRTEM image of NiO particle shown in Fig. 2(b) further suggests that the exposed crystal planes of pure NiO are dominated by {1 1 0} and {2 2 2} facets.

After the doping of manganese into NiO, the shape of NiO nanocrystals is changed, as shown in Fig. 2(c); it suggests that $MnO_x(0.13)$–NiO is in the form of nanorods with a width of approximate 5 nm and a length of 15–35 nm as well as some nanocubes with irregular shapes. Compared with the image of pure NiO, we may assume that the nanorod is Ni_6MnO_8 while
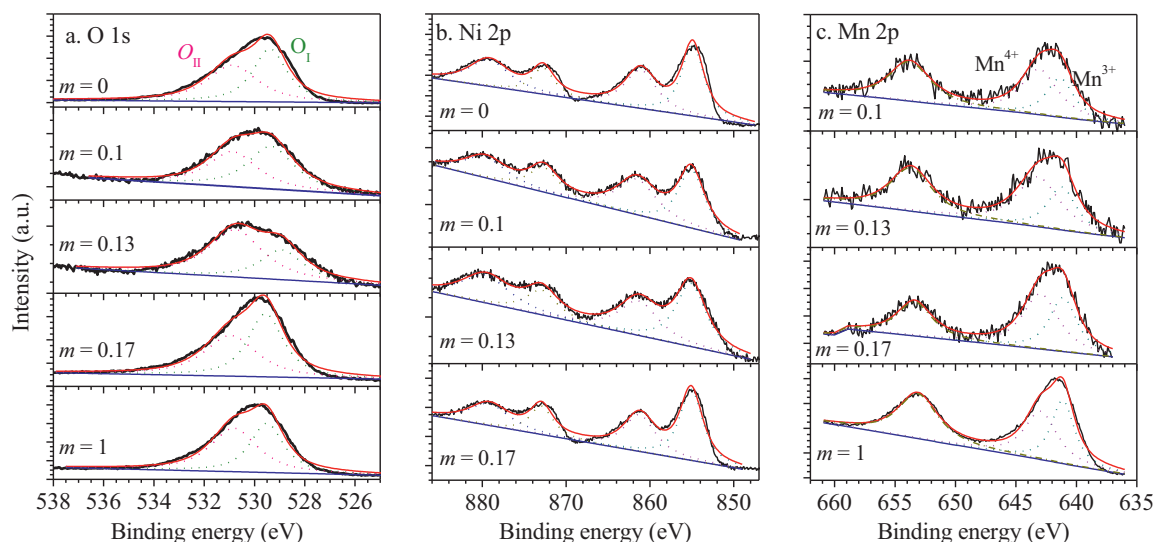
Fig. 3. XPS spectra for O 1s (a), Ni 2p (b) and Mn 2p (c) of $MnO_x(m)$–NiO composite oxides with different Mn contents.

the nanocube is NiO. This means that intermixture of MnO_x and NiO in $MnO_x(0.13)$–NiO is non-uniform and there are still a large number of congregated NiO particles. Fig. 2(d) further shows a spacing value of 0.212 nm corresponding to Ni_6MnO_8 (400) plane and a spacing value of 0.239 nm to NiO (2 2 2) in $MnO_x(0.13)$–NiO; however, no flections related to manganese species are detected. Compared with that of pure NiO (Fig. 2), the interplanar space for $MnO_x(0.13)$–NiO is decreased slightly, implying that Mn^{4+}/Mn^{3+} has inserted into the NiO crystal lattice. For pure MnO_x ($m = 1$), as shown in Fig. 2(e) and (f), the lattice spacings of 0.166 and 0.382 nm are indexed as the (4 4 0) and (2 1 1) planes of α-Mn_2O_3, respectively.

The mean particle sizes of $MnO_x(m)$–NiO estimated from the TEM images are also listed in Table 1, which give the same sequence as the crystallite sizes calculated from the XRD data, though there are some difference in the values of particle sizes determined by TEM and XRD, possibly due to the non-spherical nature of $MnO_x(m)$–NiO particles. The results of HRTEM together with XRD suggests that in $MnO_x(0.13)$–NiO, a fraction of manganese species is present as highly dispersed or amorphous manganese oxide and another fraction of manganese species may enter into the lattice of NiO. $MnO_x(0.13)$–NiO exhibits the smallest particle sizes, much smaller than NiO. These confirm that the doping of appropriate amount of manganese into NiO leads to the formation of small Mn–Ni–O solid solution particles, which is of benefit to inhibiting the growth of NiO crystallite.

3.1.2. XPS results

XPS spectra of O 1s, Ni 2p and Mn 2p are used to clarify the surface chemical composition of the $MnO_x(m)$–NiO composite oxide as well as the oxidation state of each surface species, as shown in Fig. 3 and Table 2.

The O 1s spectra (Fig. 3(a)) of $MnO_x(m)$–NiO are deconvolved into two peaks; the peak at lower binding energy (528.9–529.5 eV) corresponds to lattice oxygen (O_I), while another peak at higher binding energy (530.7–531.2 eV) may be assigned to the surface-adsorbed oxygen (O_{II}) [28]. The ratio of the surface-adsorbed oxygen to lattice oxygen (O_{II}/O_I) can be used to describe the proportion of different oxygen species [10]; higher O_{II}/O_I value implies the presence of more active vacant oxygen species on the catalyst surface. As listed in Table 2, the surface oxygen composition of $MnO_x(m)$–NiO is related to the content of manganese; $MnO_x(0.13)$–NiO has the highest surface O_{II}/O_I ratio, meaning that

it can provide the richest surface active oxygen species for the oxidation reaction.

The Ni 2p spectra (Fig. 3(b)) of $MnO_x(m)$–NiO are characterized by two main lines of Ni $2p_{3/2}$ and Ni $2p_{1/2}$ peaked at about 855 eV and 873 eV, respectively; each has an intensive shake-up satellite at higher binding energy. The doublet 2p spectra and peak binding energy values suggest that nickel in $MnO_x(m)$–NiO is mainly present as Ni^{2+}, which involves the species of NiO and/or $Ni(OH)_2$ [29]. The peak of Ni $2p_{3/2}$ for pure NiO exhibits a peak at 854.8 eV; after doping with MnO_x, it shifts to higher binding energy for $MnO_x(m)$–NiO. However, the valance of surface nickel cannot be altered through the doping of manganese. Current results are consistent with those obtained for the NiO/SiO_2–Al_2O_3 catalysts [30]. The shift towards higher binding energy can be explained by the strong interaction between Ni and Mn due to the formation of the solid solution.

The Mn 2p XPS spectra of $MnO_x(m)$–NiO, as shown in Fig. 3(c), display two peaks centered at the binding energies of 642.2 eV and 653.8 eV for Mn $2p_{3/2}$ and Mn $2p_{1/2}$, respectively, which are consistent with those reported in the literature [25,31,32]. Because various manganese species are very close in the binding energy, the broad peaks of Mn $2p_{3/2}$ can be deconvoluted into two peaks; the peak at 641.2–641.5 eV was assigned to Mn^{3+} ions and that at 642.8–643.5 eV to Mn^{4+} ions [31]. Table 2 further shows that the ratio of Mn^{4+}/Mn^{3+} in $MnO_x(m)$–NiO surface is also related to the content of manganese; $MnO_x(0.13)$–NiO exhibits the highest Mn^{4+}/Mn^{3+} ratio. It is well known that the catalytic activity of MnO_x at elevated temperatures depends strongly on the transforming ability of manganese species between different oxidation states, for example, between Mn^{2+}/Mn^{3+} or Mn^{3+}/Mn^{4+}, which reflects the "oxygen mobility" in the oxide lattice [33]. The concentration of Mn^{4+} species produced from the strong interaction between Ni and Mn are then related to oxygen mobility and activity of the $MnO_x(m)$–NiO catalyst; higher surface Mn^{4+} concentration may imply more oxygen vacancies and higher catalytic activity.

3.1.3. H_2-TPR results

The H_2-TPR profiles of $MnO_x(m)$–NiO catalysts with different Mn contents are shown in Fig. 4 and a quantitative analysis is summarized in Table 3. Pure NiO ($m = 0$) shows a reduction peak around 390 °C; this peak is attributed to the reduction of NiO to Ni [34] and is named as β peak (high temperature reduction) in this work. The presence of Ni^{3+} can be precluded in $MnO_x(m)$–NiO since no

Table 2
Surface atomic composition of $MnO_x(m)$–NiO composite oxides determined by XPS.

m	Composition (%)			Mn 2p$_{3/2}$ position (eV)		Mn/Ni ratio	Mn^{4+}/Mn^{3+} ratio	O 1s position (eV)		O_{II}/O_I ratio
	Ni	Mn	O	Mn^{3+}	Mn^{4+}			O_I	O_{II}	
0	48.7	–	51.3	–	–	0	–	529.4	530.9	1.02
0.10	30.7	8.45	60.8	641.3	643.1	0.27	1.57	529.4	530.9	1.75
0.13	31.9	10.5	57.5	641.2	643.2	0.33	1.74	528.9	530.8	2.01
0.17	30	11.3	58.8	641.1	643.0	0.38	1.38	529.6	531.0	0.95
1	–	42.5	57.5	641.2	643.2	–	1.08	529.5	530.8	1.25

Table 3
Quantitative analysis of H$_2$-TPR profiles of $MnO_x(m)$–NiO composite oxides with different Mn contents calcined at 500 °C.

m	Peak position (°C)		H$_2$ uptake (mmol/g-cat)			
	α	β	α	β	$\alpha + \beta$	$\alpha + \beta$, calculated[a]
0	–	388	–	12.1	12.1	13.3
0.10	262	410	1.2	10.6	11.8	13.2
0.13	257	412	1.9	9.1	11.0	13.0
0.17	295	435	2.0	8.6	10.6	12.9
0.25	312	462	2.3	8.1	10.4	12.8
1	328	442	2.1	3.2	5.3	11.5

[a] Theoretical H$_2$ uptake for reduction of $MnO_x(m)$–NiO, as calculated by assuming that NiO and MnO_x (as MnO_2) are stoichiometrically reduced to Ni and MnO, respectively.
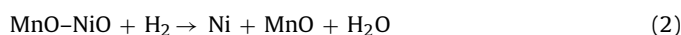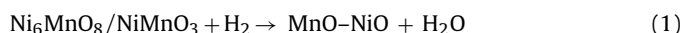
reduction peak is observed at 200 °C [35]. As listed in Table 3, the H$_2$ consumption of pure NiO (β peak) is 12.1 mmol/g, close to the theoretical value of 13.3 mmol/g for the reduction of NiO to Ni.

Pure MnO_x ($m = 1$) shows two conjoined reduction peaks, i.e. the peak at lower temperature (α, with a maximum at ca. 329 °C) and another peak at higher temperature (β, with a maximum at ca. 445 °C), which is consistent with that reported for bulk MnO_x catalyst [36]. The H$_2$ consumption of MnO_x ($\alpha + \beta$) is 5.3 mmol/g, which is much lower than the amount of hydrogen required for the stoichiometric reduction of MnO_2 to MnO (11.5 mmol/g), even lower than that required for the reduction of Mn_2O_3 to MnO (6.3 mmol/g). This may be ascribed to the poor reducibility of MnO_x, which cannot be completely reduced to MnO [17].

The reduction of bulk MnO_x may follow the sequence of $MnO_2/Mn_2O_3 \rightarrow Mn_3O_4 \rightarrow MnO$ [37,38] and the reduction of MnO to metal Mn may need a temperature above 800 °C for thermodynamic reasons [13,39]. For the two-step reduction of $MnO_2 \rightarrow Mn_3O_4 \rightarrow MnO$, the hydrogen consumption ratio of first step to second step (α/β) should be 2, while for the reduction of $Mn_2O_3 \rightarrow Mn_3O_4 \rightarrow MnO$, the ratio of α/β should be 0.5. However, an α/β ratio of 0.67 is estimated in current work for the reduction of pure MnO_x, which probably suggests that MnO_x here is a mixture

of bulk α-Mn_2O_3 and amorphous or highly dispersed MnO_2. This result is in good accordance with that reported for the reduction of bulk MnO_2/Mn_2O_3 [36,40].

After doping of manganese in NiO, the reducibility of nickel and manganese oxides species is changed. The H$_2$-TPR profile of $MnO_x(m)$–NiO exhibits two conjoined reduction peaks (α and β), which is markedly different from that of NiO (Fig. 4); the β peak area (higher reduction temperature) is much larger than the α peak area (lower reduction temperature). Moreover, with the increase of manganese content (m value) in $MnO_x(m)$–NiO, the area of α peak is increased significantly, indicating more reducible species at low temperature. As reported in the literature [41,42], the reduction of $MnO_x(m)$–NiO during H$_2$-TPR can be assumed in two steps:

$$Ni_6MnO_8/NiMnO_3 + H_2 \rightarrow MnO\text{–}NiO + H_2O \qquad (1)$$

$$MnO\text{–}NiO + H_2 \rightarrow Ni + MnO + H_2O \qquad (2)$$

During the first step, MnO_x species (as Ni_6MnO_8 or $NiMnO_3$) are reduced to Mn^{2+}, accompanied by the formation of NiO–MnO solid solution (Eq. (1)). Subsequently, Ni^{2+} is reduced into metallic nickel to form a mixture of MnO and Ni (Eq. (2)). The first reduction peak is smaller than the second peak, since the content of manganese is much lower than that of nickel in $MnO_x(m)$–NiO [25].

The reducibility of $MnO_x(m)$–NiO is related to the content of manganese. As shown in Table 3, the $MnO_x(0.13)$–NiO catalyst exhibits the lowest reduction temperature of α peak (257 °C). Meanwhile, with the increase of the manganese content, the β peak in the H$_2$-TPR profiles of $MnO_x(m)$–NiO expands to a rather broad range towards higher temperature, indicating that the reduction of NiO–MnO solid solution is becoming more difficult. Moreover, the difference between the measured and theoretical values of hydrogen uptakes for the reduction of $MnO_x(m)$–NiO is also increased with the increase of manganese content. All these may suggest that the doping of proper content of manganese (e.g. $m = 0.13$) is able to form certain easily reducible species in $MnO_x(m)$–NiO, which is of benefit to enhancing its catalytic activity for oxidation; however, the doping of excessive manganese into NiO is deleterious to the reducibility of $MnO_x(m)$–NiO.
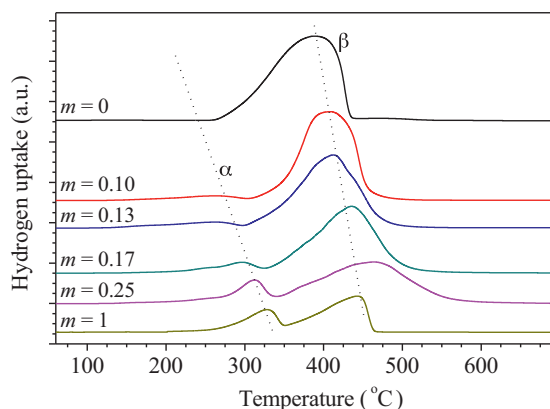
3.1.4. O$_2$-TPD results

The O$_2$-TPD profiles of $MnO_x(m)$–NiO catalysts with different Mn contents are shown in Fig. 5. For pure MnO_x ($m = 1$), a small oxygen desorption peak is observed at 563 °C; more oxygen is released again at a temperature above 750 °C. On the other side, no obvious oxygen desorption peak is observed in the O$_2$-TPD profile of pure NiO ($m = 0$), indicating that pure NiO releases little oxygen during heating, even at a temperature up to 750 °C. The oxygen desorption at low temperature (<400 °C) is generally ascribed to the surface adsorbed oxygen species (α-oxygen) such as O_2, O_2^-, and O^- adsorbed on oxygen vacancies [43], while the desorption peak at high temperature (>400 °C) can be attributed to the liberation of lattice oxygen (β-oxygen) from the bulk oxide [44].

With the doping of manganese in NiO, nickel in NiO is partially substituted by manganese, the O$_2$-TPD profiles of $MnO_x(m)$–NiO composite oxide exhibit a series of overlapped oxygen desorption peaks in the α-oxygen region. Especially for $MnO_x(0.13)$–NiO, O$_2$
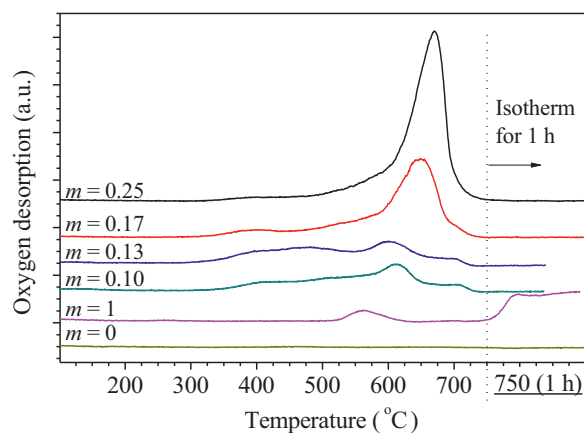

Fig. 4. H$_2$-TPR profiles of $MnO_x(m)$–NiO composite oxides with different Mn contents.

Fig. 5. O_2-TPD profiles of $MnO_x(m)$–NiO composite oxides with different Mn contents.
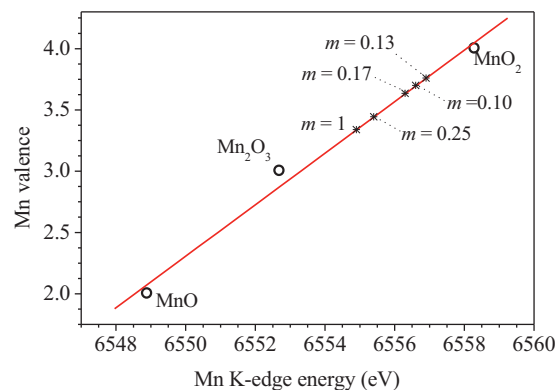

Fig. 7. Oxidation state of Mn species in $MnO_x(m)$–NiO composite oxides with different Mn contents, determined by the Mn K-edge energy shift in the XANES spectra.

desorption starts at the lowest temperature (305 °C), indicating an excellent oxygen mobility. Moreover, with the increase of the manganese content doped in NiO, the intensity of oxygen desorption peaks at high temperature (>500 °C) is markedly increased; these desorption peaks should be evoked from the lattice oxygen (β-oxygen). Current results suggest that the oxygen mobility in $MnO_x(m)$–NiO catalyst can be enhanced significantly by the doping of manganese in NiO, which are in good agreement with those reported in the literature [45,46].

On the basis of above observations, we may speculate that the doping of manganese in NiO lattice contributes to the release of α-oxygen at low temperature region, which is especially prominent for the $MnO_x(0.13)$–NiO with a proper content of manganese. For $MnO_x(m)$–NiO with higher manganese content, excessive manganese may be present as highly dispersed amorphous or crystalline Mn_2O_3, which is then decomposed to Mn_3O_4 at higher temperature and releases β-oxygen; due to the high dispersion nature of manganese species, the oxygen desorption peak here appears at a much lower temperature than that for bulk pure MnO_x. The doping of manganese in NiO can significantly promote the oxygen mobility or redox capability of $MnO_x(m)$–NiO catalyst, especially when the value of m is 0.13, which is of benefit to its performance in methane oxidation [47].

3.1.5. XAS results

The normalized Mn K-edge XANES spectra of $MnO_x(m)$–NiO and reference samples (MnO, Mn_2O_3, and MnO_2) are illustrated in Fig. 6(a). The small pre-edge peaks in XANES are attributed to the 1s–3d transition, which is sensitive to the valence of manganese atoms. $MnO_x(m)$–NiO, MnO, Mn_2O_3 and MnO_2 are quite different in the shape of their Mn K-edge XANES spectra, indicating their difference in the coordination environments of manganese. All $MnO_x(m)$–NiO samples ($m = 0.1$–0.25) here exhibit similar pre-edge features, suggesting that these samples are close in the valence of manganese species, regardless of the difference in manganese content. The energy shifts of each chemical species on the absorption edge are related to the average oxidation state of the specified atom [24]. Compared with the reference Mn_2O_3 sample, as shown in Fig. 6(a), the Mn K-edge absorption energy of $MnO_x(m)$–NiO shifts to higher value, especially for $MnO_x(0.13)$–NiO. Through calibration with the standard samples (e.g. MnO, Mn_2O_3 and MnO_2) of known oxidation state, the average oxidation state of manganese in $MnO_x(m)$–NiO can be estimated from the energy shift [48]. It is estimated that the mean oxidation state of Mn is increased from 3.36 in pure MnO_x ($m = 1$) to 3.76 in $MnO_x(m)$–NiO ($m = 0.13$), as shown in Fig. 7, which is situated at the boundary between the reference Mn_2O_3 and MnO_2 samples. This suggests that Mn species are mainly present as Mn^{3+} and Mn^{4+}. The average valence of manganese in $MnO_x(m)$–NiO is related to the content of manganese, i.e. the value of m; $MnO_x(0.13)$–NiO exhibits the highest valence
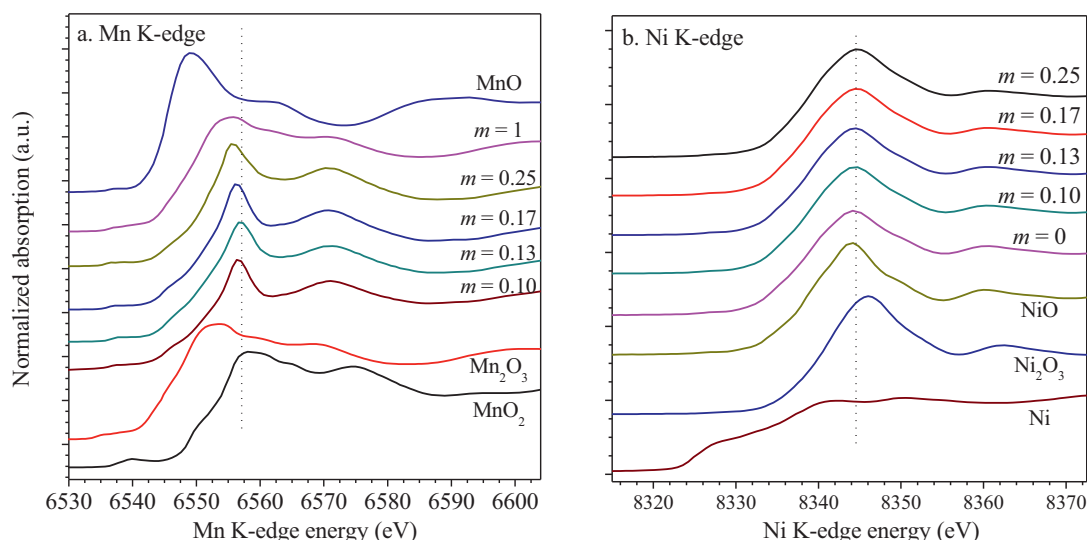

Fig. 6. Mn K-edge (a) and Ni K-edge (b) XANES spectra of $MnO_x(m)$–NiO composite oxides with different Mn contents.
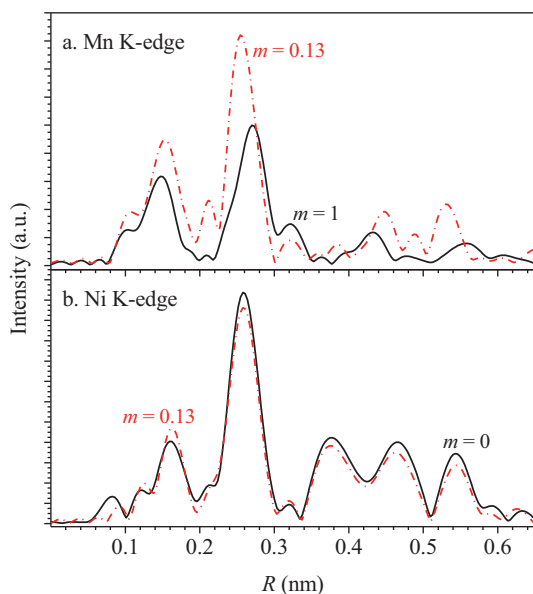
Fig. 8. Fourier transform of Mn (a) and Ni (b) K-edge EXAFS of $MnO_x(m)$–NiO composite oxides ($m = 0$, 0.13, 1).

Fig. 9. Methane conversion for the catalytic combustion over the $MnO_x(m)$–NiO composite oxides with different Mn contents.

of manganese. Such a result is consistent with that from XPS analysis (Table 2), implying that the surface composition is quite in proportion with that of the bulk $MnO_x(m)$–NiO.

Fig. 6(b) shows the normalized Ni K-edge XANES spectra of $MnO_x(m)$–NiO and reference samples (NiO, Ni_2O_3 and Ni foil). All $MnO_x(m)$–NiO samples show similar absorption spectra and characteristic edge positions of NiO, suggesting that Ni species is mainly present as Ni^{2+} with an octahedral coordination [49]. This indicates that nickel remains in the original state of Ni^{2+}, though a large portion of manganese is converted to Mn^{4+} in $MnO_x(m)$–NiO during the preparation due to the synergy of Ni and Mn.

The Mn and Ni K-edge EXAFS spectra of MnO_x, $MnO_x(0.13)$–NiO and NiO are shown in Fig. 8. MnO_x shows two major peaks at 0.15 and 0.26 nm, as shown in Fig. 8(a), which are assigned to Mn–O interaction in the first shell and Mn–Mn interaction in the second shell, respectively [50]. For $MnO_x(0.13)$–NiO, the peak at around 0.26 nm corresponding to the Mn–Mn interaction shifts to a lower distance. Since the radius of Mn^{4+} (0.056 nm) are smaller than that of Mn^{3+} (0.066 nm), this shift means the transition of Mn^{3+} to Mn^{4+} in $MnO_x(0.13)$–NiO and the extent of this shift may be an indicator for the proportion of Mn^{4+} in the composite oxide. The peak intensity of EXAFS is significantly increased for $MnO_x(0.13)$–NiO, indicating a large increase in the Mn–O and Mn–Mn coordination numbers (CN). For most of Mn^{3+}/Mn^{4+} containing substance, Mn ion is octahedrally coordinated to 6 oxygen atoms. Mn^{3+} is a Jahn–Teller distorted site; it is expected to be coordinated with oxygen in a distorted $Mn-O_6$ octahedron [51]. The oxidation of Jahn–Teller distorted Mn^{3+} to non-distorted Mn^{4+} leads to a relatively symmetric oxygen distribution, which decreases the disorder degree of local structure [52]; as a result, an increase of the EXAFS peak intensity is observed for $MnO_x(0.13)$–NiO. This is consistent with the observation by the Mn K-edge XANES that the average valence of manganese species in $MnO_x(0.13)$–NiO is higher than that in MnO_x.

Fig. 8(b) shows the Ni K-edge EXAFS spectra of $MnO_x(0.13)$–NiO and NiO. Both samples exhibit two peaks at 0.16 and 0.26 nm, which are attributed to Ni–O interaction in the first shell and Ni–Ni interactions in the second shell, respectively [53]. As shown in Fig. 8(b), $MnO_x(0.13)$–NiO and NiO are similar in the Ni–O and Ni–Ni lengths. $MnO_x(0.13)$–NiO shows a slightly higher peak intensity for Ni–O than pure NiO, suggesting a higher Ni–O coordination number in
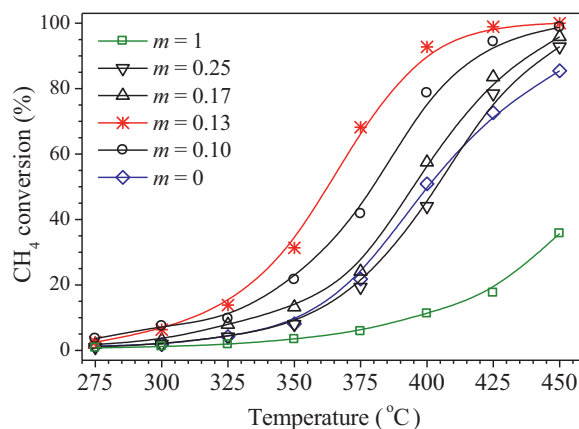
$MnO_x(0.13)$–NiO; it should be ascribed to the substitution of Ni in NiO with Mn, since Mn^{4+} is $Mn-O_6$ octahedral while NiO involves a fraction of tetrahedral NiO. Fig. 8(b) also shows that the coordination number of Ni–Ni in the second shell for $MnO_x(0.13)$–NiO is slightly lower than that for NiO, which is probably ascribed to the presence of Ni vacancies.

In summary, the XAS results for $MnO_x(m)$–NiO suggest that through the doping of proper amount of manganese in NiO, part of nickel in NiO lattice is isomorphously substituted by manganese, forming the solid solution of Mn–Ni–O. Due to the synergy interaction of Ni and Mn, manganese species in $MnO_x(0.13)$–NiO exhibits a higher valence and coordination number than that in MnO_x; moreover, nickel vacancies may appear in the second cationic coordination shell in the $MnO_x(0.13)$–NiO composite oxide.

3.2. Catalytic performance of $MnO_x(m)$–NiO in methane combustion

The catalytic performance of $MnO_x(m)$–NiO composite oxide in lean methane combustion evaluated under oxygen-rich conditions are shown in Fig. 9. During these tests, it is found that the combustion products involve only CO_2 and H_2O, suggesting an excellent selectivity for the $MnO_x(m)$–NiO composite oxide in the complete oxidation of methane.

As shown in Fig. 9, pure MnO_x exhibits the lowest activity for the catalytic combustion of lean methane among the catalysts tested; at 450 °C, methane conversion over MnO_x is only 35.7%. Over pure NiO, methane conversion is 85.4% at 450 °C. After the doping of manganese into NiO, the catalytic activity of $MnO_x(m)$–NiO composite oxide in lean methane combustion is markedly enhanced; the conversion of methane over $MnO_x(m)$–NiO at given temperature is much higher than that over pure NiO or MnO_x. Meanwhile, the extent of this activity enhancement by doping Mn in NiO is related to the content of manganese in $MnO_x(m)$–NiO. Fig. 9 shows that the activity of the catalysts tested here is in the order of $MnO_x(0.13)$–NiO > $MnO_x(0.10)$–NiO > $MnO_x(0.17)$–NiO > MnO_x (0.25)–NiO > NiO > MnO_x. It is interesting to note that the activity of $MnO_x(m)$–NiO catalysts with different manganese contents follows the same sequence as that of the Mn^{4+}/Mn^{3+} ratio in the catalysts as estimated by the XPS and XAS analysis. These may suggest that the coupling of Mn^{4+}/Mn^{3+} plays an important role in the oxidation of methane. For the combustion of methane over manganese–lanthanum oxides modified with silver, Machocki et al. [17] reported that a large number of manganese ions in the unstable oxidation state (Mn^{4+}) are obtained by filling up the oxygen vacancies and the ratio of Mn^{4+}/Mn^{3+} on catalyst surface was related to the catalytic activity.

Table 4
Catalytic activity of various materials for the lean methane combustion as indicated by the temperature needed for a methane conversion of 90% (T_{90}).

Catalyst	T_{90} (°C)	Reaction conditions	Reference
5 wt.% Pd/MgAlO$_2$	477	CH_4(1%)/air; 20 000 h^{-1}	[54]
2 wt.% Pd/LaFeO$_3$	460	CH_4(1%)/O$_2$(4.4%)/He; 18 400 h^{-1}	[55]
2 wt.% Pd/HZSM-5	500	CH_4(1%)/O$_2$(4%)/N$_2$; 15 000 h^{-1}	[56]
Mn$_{0.3}$Ce$_{0.7}$/Al$_2$O$_3$	465	CH_4(20%)/O$_2$(40%)/Ar; 30 000 ml h^{-1} g^{-1}	[57]
α-Mn$_2$O$_3$	650	CH_4(0.5%)/O$_2$(3%)/He; 36 000 h^{-1}	[58]
Mn$_{0.6}$Ce$_{0.4}$O$_2$	580	CH_4(0.5 kPa)/O$_2$(3 kPa)/Ar; 36 000 h^{-1}	[59]
MnO$_x$(0.13)–NiO	396	CH_4(1%)/O$_2$(19%)/Ar; 30 000 ml h^{-1} g^{-1}	This work

MnO$_x$(0.13)–NiO exhibits the highest activity in the lean methane combustion; over it methane conversion reaches 96% at 396 °C and 100% at 450 °C. Excessive amount of manganese in MnO$_x$(m)–NiO may reduce its activity in the lean methane combustion. Moreover, compared with some other catalysts reported in the literature for the lean methane combustion [54–59], as listed in Table 4, the MnO$_x$(0.13)–NiO catalyst also exhibits much higher activity, which is rarely observed for a non-noble metal catalyst and even comparable to some noble metal catalysts.

MnO$_x$(0.13)–NiO catalyst performs outstandingly in the lean methane combustion, which can be explained by above characterization results. Through the doping of proper content of manganese in NiO, the MnO$_x$(0.13)–NiO catalyst as a Ni–Mn–O solid solution is provided with abundant highly dispersed manganese species of higher valence (Mn^{4+}) and higher coordination number as well as certain nickel vacancies, due to the synergy interaction of nickel and manganese species. Figueroa et al. [24] explained the catalytic activity from the view of electronic theory; the presence of Mn^{3+} ions, Mn^{4+} ions, as well as Ni^{2+} vacancies improved the electronic conductivity, which might benefit to its catalytic performance. The presence of abundant Mn^{4+} species is also helpful to provide active oxygen species [17,33]; as a result, the oxygen mobility and redox capacity of the MnO$_x$(0.13)–NiO composite oxide are improved. All these may contribute to the excellent performance of MnO$_x$(0.13)–NiO catalyst in lean methane oxidation.

4. Conclusions

A series of MnO$_x$(m)–NiO composite oxide catalysts with different compositions were prepared by co-precipitation method. Compared with the corresponding single NiO and MnO$_x$ oxides, the MnO$_x$(m)–NiO composite oxide with proper composition exhibits much higher catalytic performance in the combustion of lean methane at low temperature. The activity of MnO$_x$(m)–NiO catalysts is related to the content of manganese in MnO$_x$(m)–NiO; MnO$_x$(0.13)–NiO with an atomic ratio of n(Mn)/(n(Mn) + n(Ni)) being 0.13 performs best in the lean methane combustion; methane conversion over MnO$_x$(0.13)–NiO reaches 96% at 396 °C and 100% at 450 °C, which is outstanding as a non-noble catalyst compared with those reported in the open literature.

The excellent performance of MnO$_x$(m)–NiO catalysts were explained by various characterizations like XRD, XPS, H$_2$-TPR, O$_2$-TPD, XAS, etc. The results suggest that the doping of appropriate amount of manganese into NiO leads to the formation of small Mn–Ni–O solid solution particles, which is of benefit to inhibiting the growth of NiO crystallite. Through the doping of proper content of manganese in NiO, the MnO$_x$(0.13)–NiO catalyst as a Ni–Mn–O solid solution is provided with abundant highly dispersed manganese species of higher valence (Mn^{4+}) and higher coordination number as well as certain nickel vacancies, due to the synergy interaction of nickel and manganese. These are helpful to provide active oxygen species as well as to improve the oxygen mobility and redox capacity of MnO$_x$(0.13)–NiO. All these may contribute to the excellent performance of MnO$_x$(0.13)–NiO catalyst in the lean methane oxidation.

References

[1] M.N. Debbagh, C.S.M. de Lecea, J. Pérez-Ramírez, Applied Catalysis B: Environmental 70 (2007) 335–341.
[2] US Environmental Protection Agency (EPA) reports, Assessment of the Worldwide Market Potential for Oxidizing Coal Mine Ventilation Air Methane, 2003, see the website of http://www.epa.gov
[3] The Global Methane Initiative (GMI) reports, Global Methane Emissions and Mitigation Opportunities, 2010, see the website of http://www.globalmethane.org
[4] Z. Jiang, J. Yu, J. Cheng, T. Xiao, M.O. Jones, Z. Hao, P.P. Edwards, Fuel Processing Technology 91 (2010) 97–102.
[5] D. Qiao, G. Lu, D. Mao, X. Liu, H. Li, Y. Guo, Y. Guo, Catalysis Communications 11 (2010) 858–861.
[6] N. van Vegten, T. Baidya, F. Krumeich, W. Kleist, A. Baiker, Applied Catalysis B: Environmental 97 (2010) 398–406.
[7] Z. Wang, Y. Liu, P. Shi, C.J. Liu, Y. Liu, Applied Catalysis B: Environmental 90 (2009) 570–577.
[8] O. Demoulin, B. Le Clef, M. Navez, P. Ruiz, Applied Catalysis A: General 344 (2008) 1–9.
[9] X. Guo, G. Zhi, X. Yan, G. Jin, X. Guo, P. Brault, Catalysis Communications 12 (2011) 870–874.
[10] J. Li, X. Liang, S. Xu, J. Hao, Applied Catalysis B: Environmental 90 (2009) 307–312.
[11] X.G. Ren, J.D. Zheng, Y.J. Song, Journal of Fuel Chemistry and Technology 39 (2011) 717–720.
[12] R. Craciun, B. Nentwick, K. Hadjiivanov, H. Knozinger, Applied Catalysis A: General 243 (2003) 67–79.
[13] M.R. Morales, B.P. Barbero, L.E. Cadús, Applied Catalysis B: Environmental 67 (2006) 229–236.
[14] Y.-F. Han, L. Chen, K. Ramesh, E. Widjaja, S. Chilukoti, I.K. Surjami, J. Chen, Journal of Catalysis 253 (2008) 261–268.
[15] J.Q. Torres, J.-M. Giraudon, J.-F. Lamonier, Catalysis Today 176 (2011) 277–280.
[16] V.R. Choudhary, B.S. Uphade, S.G. Pataskar, Applied Catalysis A: General 227 (2002) 29–41.
[17] A. Machocki, T. Ioannides, B. Stasinska, W. Gac, G. Avgouropoulos, D. Delimaris, W. Grzegorczyk, S. Pasieczna, Journal of Catalysis 227 (2004) 282–296.
[18] N. Bahlawane, Applied Catalysis B: Environmental 67 (2006) 168–176.
[19] E. Heracleous, A.A. Lemonidou, Journal of Catalysis 237 (2006) 162–174.
[20] Z. Wu, H. Zhu, Z. Qin, H. Wang, J. Ding, L. Huang, J. Wang, Fuel, in press
[21] F. Kovanda, T. Grygar, V. Dornicák, Solid State Sciences 5 (2003) 1019–1026.
[22] T. Ressler, Journal of Synchrotron Radiation 5 (1998) 118–122.
[23] T. Ressler, J. Wong, J. Roos, I.L. Smith, Environmental Science and Technology 34 (2000) 950–958.
[24] S.J.A. Figueroa, F.G. Requejo, E.J. Lede, L. Lamaita, M.A. Peluso, J.E. Sambeth, Catalysis Today 107–108 (2005) 849–855.
[25] D. Delimaris, T. Ioannides, Applied Catalysis B: Environmental 84 (2008) 303–312.
[26] J. Trawczyński, B. Bielak, W. Miśta, Applied Catalysis B: Environmental 55 (2005) 277–285.
[27] P. Porta, G. Minelli, I.L. Botto, E.J. Baran, Journal of Solid State Chemistry 92 (1991) 202–207.
[28] X. Tang, Y. Li, X. Huang, Y. Xu, H. Zhu, J. Wang, W. Shen, Applied Catalysis B: Environmental 62 (2006) 265–273.
[29] N.V. Kosova, E.T. Devyatkina, V.V. Kaichev, Journal of Power Sources 174 (2007) 735–740.
[30] S.R. Kirumakki, B.G. Shpeizer, G.V. Sagar, K.V.R. Chary, A. Clearfield, Journal of Catalysis 242 (2006) 319–331.

[31] H. Li, G. Lu, Q. Dai, Y. Wang, Y. Guo, Y. Guo, Applied Catalysis B: Environmental 102 (2011) 475–483.

[32] S. Todorova, H. Kolev, J.P. Holgado, G. Kadinov, C. Bonev, R. Pereñíguez, A. Caballero, Applied Catalysis B: Environmental 94 (2010) 46–54.

[33] H. Pérez, P. Navarro, J.J. Delgado, M. Montes, Applied Catalysis A: General 400 (2011) 238–248.

[34] M. Koike, C. Ishikawa, D. Li, L. Wang, Y. Nakagawa, K. Tomishige, Fuel, in press

[35] B. Mile, D. Stirling, M.A. Zammitt, A. Lovell, M. Webb, Journal of Molecular Catalysis 62 (1990) 179–198.

[36] J. Trawczynski, B. Bielak, W. Mista, Applied Catalysis B: Environmental 55 (2005) 277–285.

[37] M.C. Álvarez-Galván, V.A. de la Peña O'Shea, J.L.G. Fierro, P.L. Arias, Catalysis Communications 4 (2003) 223–228.

[38] M.J. Keyser, R.C. Everson, R.L. Espinoza, Applied Catalysis A: General 171 (1998) 99–107.

[39] N. Yamazoe, Y. Teraoka, Catalysis Today 8 (1990) 175–199.

[40] X. Wang, Q. Kang, D. Li, Catalysis Communications 9 (2008) 2158–2162.

[41] L. Christel, A. Pierre, D.A.-M.R. Abel, Thermochimica Acta 306 (1997) 51–59.

[42] C. Laberty, J. Pielaszek, P. Alphonse, A. Rousset, Solid State Ionics 110 (1998) 293–302.

[43] M.R. Morales, B.P. Barbero, L.E. Cadús, Applied Catalysis B: Environmental 74 (2007) 1–10.

[44] L. Xue, C. Zhang, H. He, Y. Teraoka, Applied Catalysis B: Environmental 75 (2007) 167–174.

[45] Q. Zhang, X. Liu, W. Fan, Y. Wang, Applied Catalysis B: Environmental 102 (2011) 207–214.

[46] D. Döbber, D. Kießling, W. Schmitz, G. Wendt, Applied Catalysis B: Environmental 52 (2004) 135–143.

[47] J. Chen, W. Shi, J. Li, Catalysis Today 175 (2011) 216–222.

[48] A. Campos, N. Lohitharn, A. Roy, E. Lotero, J.G. Goodwin Jr., J.J. Spivey, Applied Catalysis A: General 375 (2010) 12–16.

[49] Q. Tang, C. Wu, R. Qiao, Y. Chen, Y. Yang, Applied Catalysis A: General 403 (2011) 136–141.

[50] I. Nakai, K. Yasaka, H. Sasaki, Y. Terada, H. Ikuta, M. Wakihara, Journal of Power Sources 97–98 (2001) 412–414.

[51] Y. Shiraishi, I. Nakai, T. Tsubata, T. Himeda, F. Nishikawa, Journal of Solid State Chemistry 133 (1997) 587–590.

[52] K.-W. Nam, M.G. Kim, K.-B. Kim, Journal of Physical Chemistry C 111 (2006) 749–758.

[53] L. Huang, G. Wang, Z. Qin, M. Dong, M. Du, H. Ge, X. Li, Y. Zhao, J. Zhang, T. Hu, J. Wang, Applied Catalysis B: Environmental 106 (2011) 26–38.

[54] S. Tanasoi, G. Mitran, N. Tanchoux, T. Cacciaguerra, F. Fajula, I. Sandulescu, D. Tichit, I.-C. Marcu, Applied Catalysis A: General 395 (2011) 78–86.

[55] A. Eyssler, A. Winkler, P. Mandaliev, P. Hug, A. Weidenkaff, D. Ferri, Applied Catalysis B: Environmental 106 (2011) 494–502.

[56] C.-j. Liu, K. Yu, Y.-P. Zhang, X. Zhu, F. He, B. Eliasson, Applied Catalysis B: Environmental 47 (2004) 95–100.

[57] L. Shi, W. Chu, F. Qu, J. Hu, M. Li, Journal of Rare Earths 26 (2008) 836–840.

[58] Y.-F. Han, K. Ramesh, L. Chen, E. Widjaja, S. Chilukoti, F. Chen, Journal of Physical Chemistry C 111 (2007) 2830–2833.

[59] J. Xu, P. Li, X. Song, C. He, J. Yu, Y.-F. Han, Journal of Physical Chemistry Letters 1 (2010) 1648–1654.